

The circumstellar disk, envelope, and bi-polar outflow of the Massive Young Stellar Object W33A

Ben Davies^{1,2}, Stuart L. Lumsden¹, Melvin G. Hoare¹, René D. Oudmaijer¹,
Willem-Jan de Wit¹

¹*School of Physics & Astronomy, University of Leeds, Woodhouse Lane, Leeds LS2 9JT, UK*

²*Chester F. Carlson Center for Imaging Science, Rochester Institute of Technology, 54 Lomb Memorial Drive, Rochester, NY 14623, USA*

Accepted ... Received ...

ABSTRACT

The Young Stellar Object (YSO) W33A is one of the best known examples of a massive star still in the process of forming. Here we present Gemini North ALTAIR/NIFS laser-guide star adaptive-optics assisted K -band integral-field spectroscopy of W33A and its inner reflection nebula. In our data we make the first detections of a rotationally-flattened outer envelope and fast bi-polar jet of a massive YSO at near-infrared wavelengths. The predominant spectral features observed are Br γ , H₂, and a combination of emission and absorption from CO gas. We perform a 3-D spectro-astrometric analysis of the line emission, the first study of its kind. We find that the object's Br γ emission reveals evidence for a fast bi-polar jet on sub-milliarcsecond scales, which is aligned with the larger-scale outflow. The hybrid CO features can be explained as a combination of hot CO emission arising in a disk close to the central star, while cold CO absorption originates in the cooler outer envelope. Kinematic analysis of these features reveals that both structures are rotating, and consistent with being aligned perpendicularly to both the ionised jet and the large-scale outflow. Assuming Keplerian rotation, we find that the circumstellar disk orbits a central mass of $\gtrsim 10M_{\odot}$, while the outer envelope encloses a mass of $\sim 15M_{\odot}$. Our results suggest a scenario of a central star accreting material from a circumstellar disk at the centre of a cool extended rotating torus, while driving a fast bi-polar wind. These results therefore provide strong supporting evidence for the hypothesis that the formation mechanism for high-mass stars is qualitatively similar to that of low-mass stars.

Key words: ISM: individual: W33a – stars: pre-main-sequence – ISM: HII regions

1 INTRODUCTION

It is still unclear how massive stars ($M_{*} \gtrsim 8M_{\odot}$) are formed. This is due in part to the rapid formation timescales of such stars ($\lesssim 10^5$ yrs), which mean that the star can reach the main-sequence (MS) while it is still heavily embedded in its natal molecular cloud. Also, it is still unknown how a massive protostar can continue to accrete despite the immense outward radiation pressure it exerts on its surroundings (for reviews of massive star formation see e.g. Beuther et al. 2007; Hoare et al. 2007).

It has been suggested that massive stars may form through a mechanism similar to that of lower mass stars, whereby matter is accreted from a circumstellar disk, with the outward radiative force escaping via the poles and driving a fast bipolar wind. Several numerical studies have succeeded in creating stars with masses $\gtrsim 30M_{\odot}$ this way (e.g. Yorke & Sonnhalter 2002; Krumholz et al. 2009), while

it has been shown that the fast bipolar winds should strongly influence the infalling material from the envelope (Parkin et al. 2009). The observational evidence to support this scenario however is limited and circumstantial. The CO bandhead emission at $2.3\mu\text{m}$ has been modelled as arising in a circumstellar disk (e.g. Chandler et al. 1993, 1995; Bik & Thi 2004a; Blum et al. 2004); large-scale bipolar outflows have been observed to originate from heavily embedded objects (e.g. Beuther et al. 2002); and some authors have found evidence of accretion disks in individual massive protostars (Patel et al. 2005; Beltrán et al. 2006; Torrelles et al. 2007).

Massive Young Stellar Objects (MYSOs) are thought to represent the phase in a massive star's formation immediately before the star reaches the main-sequence (MS) but whilst it is still accreting, and as such are important objects with which to study the formation of massive stars. W33A

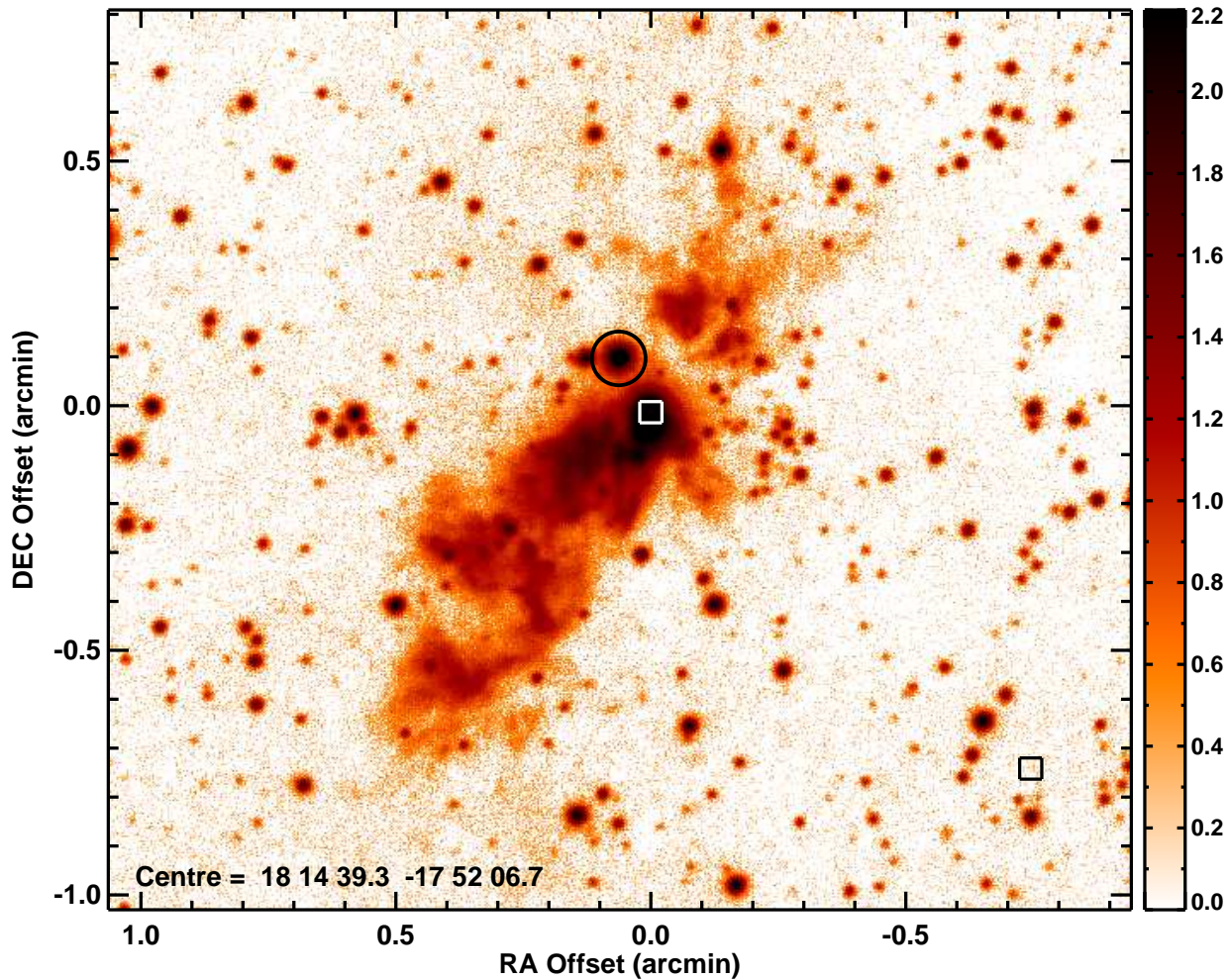


Figure 1. Wide-field K -band image of W33A, taken from the UKIDSS Galactic Plane Survey (Lucas et al. 2008). The image is logarithmically scaled in units of sigma above the background. The NIFS field-of-view is indicated by the white box. Our sky field is indicated by the black box in the lower-right of the image. The natural guide star, used in the tip-tilt correction stage of the adaptive optics system, is indicated by the black circle.

is a well-known MYSO. It lies at a distance of ~ 3.8 kpc and has a source luminosity of $\sim 10^5 L_{\odot}$ (Faúndez et al. 2004). It is deeply embedded (e.g. Gibb et al. 2000), but is visible in the K band despite this. The morphology of the object’s large-scale nebula suggests a bipolar outflow, but as yet no convincing evidence exists for an accretion disk or a bipolar wind close to the central star. The object’s weak radio emission has only been marginally resolved at radio wavelengths (Rengarajan & Ho 1996; van der Tak & Menten 2005). The close environment of W33A has been probed using mid-IR interferometry (de Wit et al. 2007, de Wit et al. 2009, submitted), with the visibilities well fitted by a model in which the emission arises in the warm dusty envelope close to the surface of the cavity created by a bipolar outflow.

To provide a detailed study of W33A’s inner nebula, and ultimately to investigate the physical processes occurring in the formation of the central star, in this paper we present high spatial resolution integral field spectroscopy of W33A. These data allow us to study the spatial variations in emission from the ionised outflow, the dense, hot molecular

material close to the star, and the cooler molecular material in the object’s inner envelope and outflow.

We begin in Sect. 2 with a description of the observations and data reduction steps. We present the results of the data in Sect. 3, and provide a discussion in Sect. 4. We conclude in Sect. 5.

2 OBSERVATIONS & DATA REDUCTION

2.1 Observations

In Fig. 1 we show the wide-field K -band image of the W33A region taken from the UKIDSS Galactic Plane Survey (Lucas et al. 2008). The image clearly shows what appears to be a large-scale outflow extending $\sim 0.8'$ towards the south-east at a position-angle (PA) measured to be $(135 \pm 5)^{\circ}$. Diffuse emission is also seen to the north-west of the flux peak, which may be the opposite lobe of the outflow. A velocity resolved ^{12}CO map of this region conclusively shows that the material is outflowing from the central source (see Fig. 2 of de Wit et al., submitted).

Our data were taken using the Gemini Near-infrared Integral Field Spectrograph (NIFS, McGregor et al. 2003) on the nights of 16 April and 25 May 2008. The observations were pointed such that the bright flux centre was at the northern edge of the instrument field-of-view, in order to obtain data on the base of the outflow as well as the central source. The instrument applies the image-slicing technique to separate the $3'' \times 3''$ field-of-view into 29 slices, which are then aligned on the detector and passed through a diffraction grating. We employed the K grating in combination with the HK filter and central wavelength set at $2.2\mu\text{m}$. This setup achieved a spectral resolution of $R \approx 5300$ over the wavelength range $2.0\text{--}2.4\mu\text{m}$ across the full NIFS field-of-view.

Our observations made use of the Gemini ALTAIR laser-guide star (LGS) adaptive optics system. The system uses a natural guide star for tip-tilt correction, and the laser guide star for wavefront sensing. For tip-tilt correction we used the star 2UCAC-25155527, which has $m_{\text{UC}} = 14.6$ and is located $6.9''$ from the centre of our field-of-view (see Fig. 1).

The observational strategy involved observing the target and neighbouring sky in an ABBA pattern, the location of the sky field is shown in Fig. 1. The integration time per individual observation was 180s, with each integration read-out in the FAINT_MODE setting of 16 non-destructive reads. A total of 7 separate integrations were used, giving a total integration time of ~ 20 mins. In addition to the science target, we observed the A0 V double HR6798 to characterize the telluric absorption. The GCAL calibration unit was used to take continuum lamp observations plus associated dark frames for flat-fielding purposes. Argon-Xenon arc exposures were obtained for wavelength calibration, as well as ronchi flats which are used to characterize the spatial distortion of NIFS data.

2.2 Data reduction

The preliminary stages of data-reduction were done using the Gemini instrument-specific pipeline which runs on the IRAF platform. Science observations had their associated sky frames subtracted to remove the dark current and sky emission lines. The data were then divided through by the normalized flat-field to correct for pixel-to-pixel variations in sensitivity, and any bad pixels flagged in the earlier reduction steps were interpolated over. The arc and ronchi flat frames were used to derive the transformation matrix of the 2-dimensional ‘sliced’ image onto a 3-dimensional (x, y, λ) datacube. The application of this transformation rectifies the data both spatially and spectrally, and it is at this step that the wavelength calibration is applied.

Removal of telluric absorption and combination of the individual datacubes was done in IDL, using custom-written routines and the GSFC IDL library¹. Correction for the Br γ absorption in the telluric standard was done by dividing through by a synthetic AO V template spectrum, interactively altering the centroid and absorption strength of the Br γ feature in the template until a satisfactory match to

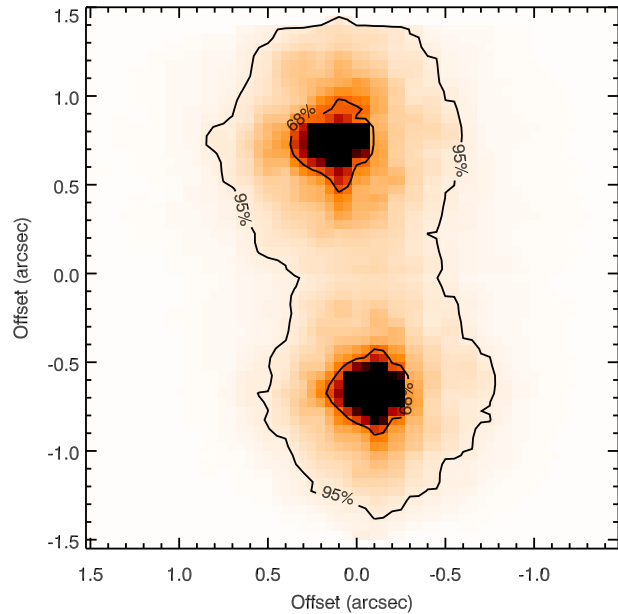


Figure 2. Image of the A0 v double HR6798A+B, illustrating the performance of the ALTAIR-LGS adaptive optics system during the observations. Contours show the encircled energy at 68% and 95% of the total flux. The FWHM was measured as $0.13''$.

the standard star was found. At each spatial pixel of the science datacube, the spectrum was extracted and divided by the telluric standard. If the spectrum had sufficient signal-to-noise (i.e. over ~ 100 counts in the continuum) the two spectra were first cross-correlated to achieve optimal telluric correction, particularly important in the region of the OH absorption lines at $2.0\text{--}2.1\mu\text{m}$ where sub-pixel misalignments can introduce artifacts into the spectrum.

The individual science datacubes of repeat observations were spatially aligned by first taking the median image of each cube across all spectral pixels, then cross-correlating these median images with one another. We then took the sum of the spectra at each spatial pixel, using the median of these spectra as a template from which to reject any further bad pixels and cosmic-ray hits.

2.3 Adaptive optics performance

In order to illustrate the spatial resolution of the data and the PSF correction that was achieved through the ALTAIR adaptive optics system, in Fig. 2 we show the wavelength-integrated image of the telluric standard stars HR6798A+B. To better demonstrate the shape and size of the corrected PSF, the image was first split into two, with each sub-image containing one star. The sub-images were normalized such that the corrected flux from each star was the same, then the sub-images were recombined. On the image we have drawn contours indicating 67% and 95% encircled energy. While the star to the north appears slightly elliptical, the southern star is circular to within the errors. For each star we find 67% of the PSF flux is contained within a radius of $\approx 0.15''$ of the flux centre. The full-width half-maximum (FWHM) of each star was measured to be $0.13''$.

¹ <http://idlastro.gsfc.nasa.gov>

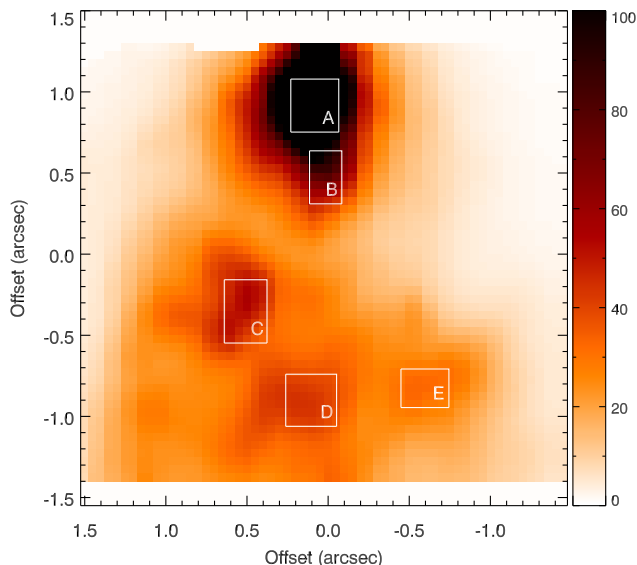


Figure 3. NIFS K-band image of W33A when integrated over all spectral channels, with North up and East to the left. The image is scaled in units of sigma above the background, estimated from the NW corner of the field. The location of maximum flux is labelled ‘A’, and the other four bright knots of emission are labelled ‘B’-‘E’.

2.4 Variations in spectral resolution and wavelength calibration

The accuracy of the wavelength calibration and the consistency of spectral resolution was determined from analysis of datacubes constructed from the arc lamp observations. For each arc line that was used to determine the wavelength solution we fitted gaussian line profiles, and measured the line-width and velocity offset. We found that the absolute wavelength calibration had a root-mean-square standard deviation of $\pm 4 \text{ km s}^{-1}$ across the field-of-view, with no discernable trends with spatial position. The spectral resolution was similarly found to be $\Delta v = 55 \pm 4 \text{ km s}^{-1}$ across the field, again having no trend with spatial position, other than that it was systematically poorer by $\sim 6 \text{ km s}^{-1}$ in the south-east $0.5'' \times 0.5''$ region. As very little data was used from this region, we did not correct for this effect.

3 RESULTS

3.1 Nebular morphology

In Fig. 3 we show the total two-dimensional image when the datacube is summed across all wavelength channels. The central source is not a point-source, and instead is noticeably extended in the north-south direction (see Fig. 4). In particular, we see a bright central peak (labelled ‘A’ in Fig. 3) and a ‘finger’ pointing southward (labelled as ‘B’). The ‘L’-shaped inner nebula, which can be marginally resolved in the UKIDSS *K*-band image and which forms the base of the outflow, is resolved in our data into three bright knots of emission, which we label ‘C’, ‘D’ and ‘E’. As we show later, the emission from these knots is predominantly scattered light.

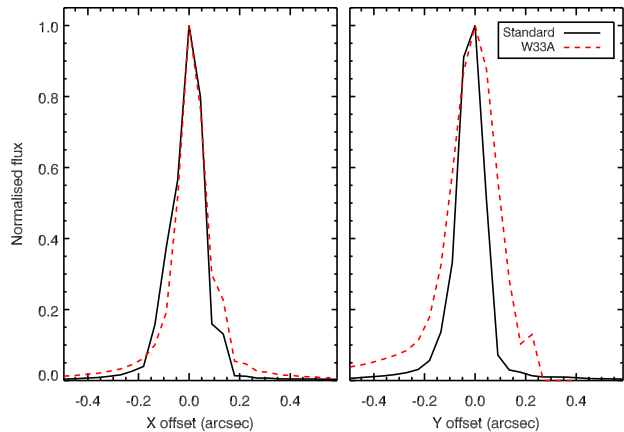


Figure 4. Spatial profile of the flux centroid of W33A when compared to the average profile of the two standard stars. While the profiles in the *x*-direction are similar, the *y*-profile of W33A is noticeably extended in comparison to the standard.

Table 1. Equivalent widths of the atomic emission lines. The uncertainty on EW was measured from fluctuations in the continuum.

Line	λ_{vac}	EW (Å)
Br γ	2.1662	-5.00 ± 0.17
Mg II	2.1374	-0.43 ± 0.17
Mg II	2.1438	-0.24 ± 0.17
Na I	2.2062	-0.50 ± 0.17
Na I	2.2090	-0.37 ± 0.17

3.2 Spatial variations of spectral properties

The unique feature of IFU data is that it is possible to chart the variations of the observed spectral properties across the field of view. We begin in this section with a description of the principle spectral features, followed by an analysis of how these features vary with spatial position.

In Fig. 5 we plot the spectrum of the bright central source extracted from region A (see Fig. 3). The steeply-rising continuum indicates that the central source is heavily reddened. In order to highlight the spectral features, in the bottom panel of the figure we show the spectrum when normalized by a 4th-degree polynomial fit to the continuum (labelled as ‘region A’ in the Figure). In this normalised spectrum we see emission features of Br γ , H₂, Na I and the CO 2-0, 3-1, 4-2 and 5-3 bandheads. Also seen are narrow absorption lines in the region of the CO bandheads, attributable to low *J* transitions of the CO $v=2-0$ state, as well as a broad absorption feature around $2.28 \mu\text{m}$ which we attribute to CH₃OH ice (also observed in this object’s spectrum by Taban et al. 2003). We do not confirm the presence of He I emission detected by Taban et al. (2003), while there is a suggestion of emission from the Mg II doublet at $2.14 \mu\text{m}$. Table 1 shows the measured equivalent widths of the atomic emission lines as measured from the region A aperture.

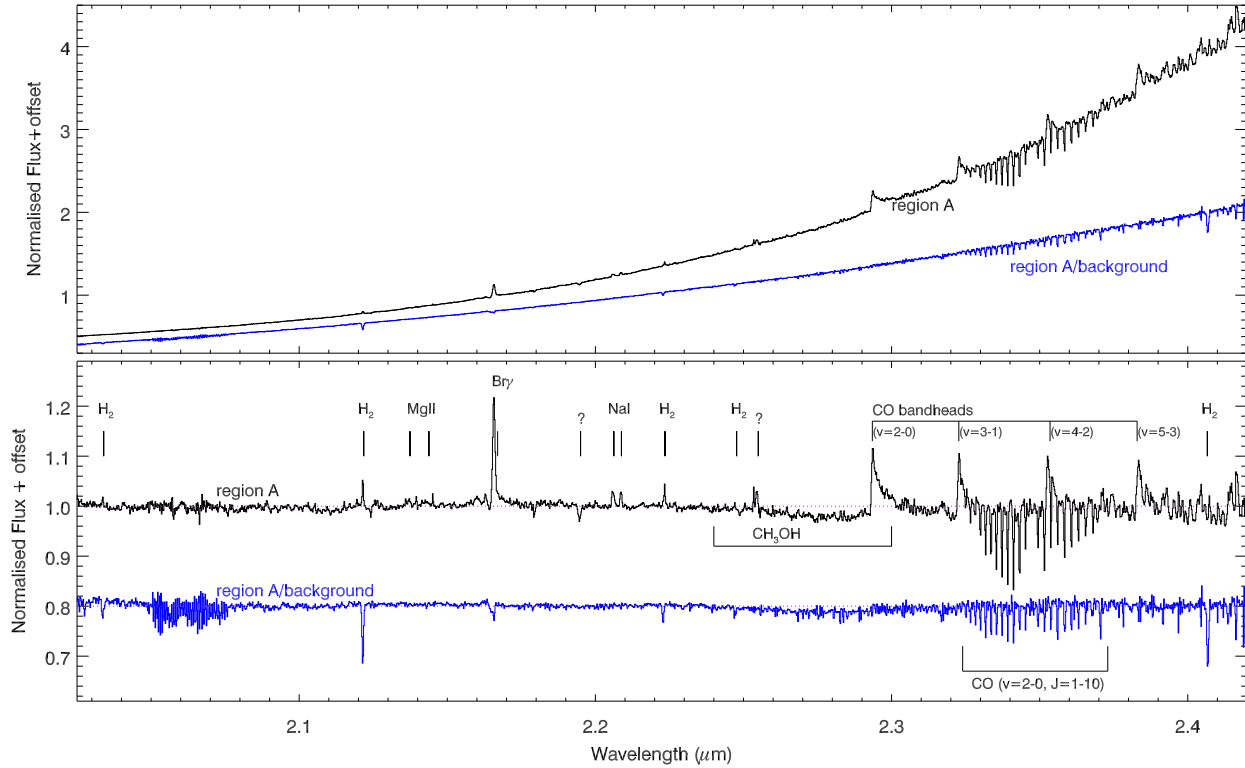


Figure 5. Spectrum of region A, and the ratio of region A’s spectrum to that of the average background spectrum. The top panel shows the spectra before continuum fitting, to illustrate the high degree of reddening. The bottom panel shows the spectra after dividing through by fits to the continua, to highlight the discrete spectral features.

3.2.1 Spectrum of the central source versus surrounding nebula

To analyse spectral differences between region A and the rest of the field, we have created an average ‘background’ spectrum by integrating over all spatial pixels in the observed field *except* those in region A. In the top panel of Fig. 5 we have also plotted the ratio of the region A spectrum to this background spectrum, labelled ‘region A/background’. The continuum of this ratio spectrum is shallower than that of the central source, which is to be expected if the emission in the southern nebula is predominantly scattered light.

In the bottom panel of Fig. 5 we plot the ratio of the spectra when normalized by a continuum fit. Here the emission due to Br γ , NaI, MgII and CO disappears, suggesting that the emission morphologies of these features follow that of the continuum, i.e. they are also scattered. The H₂ lines go into ‘absorption’ indicating that this emission originates mainly in the surrounding nebula rather than on the bright source at region A. The CH₃OH and CO absorption are still seen in the residual spectrum, implying that there is an increased level of opacity due to these features along the line-of-sight to region A compared with the surrounding nebula.

3.2.2 Variations in continuum emission

In the previous section we showed that the slope of the *K*-band continuum emission is not uniform across the field. To

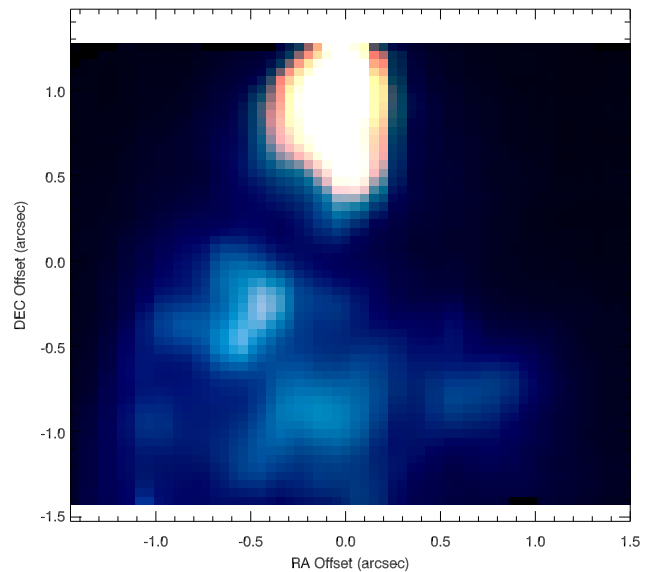


Figure 6. Three-colour image of the continuum emission. Each RGB channel is scaled linearly, while the dynamic ranges were chosen arbitrarily to best illustrate the contrast between region A and the southern nebula.

further illustrate the spatial variations in continuum emission we created narrow band continuum images at three featureless regions of the spectrum: 2.083 μ m, 2.185 μ m, and

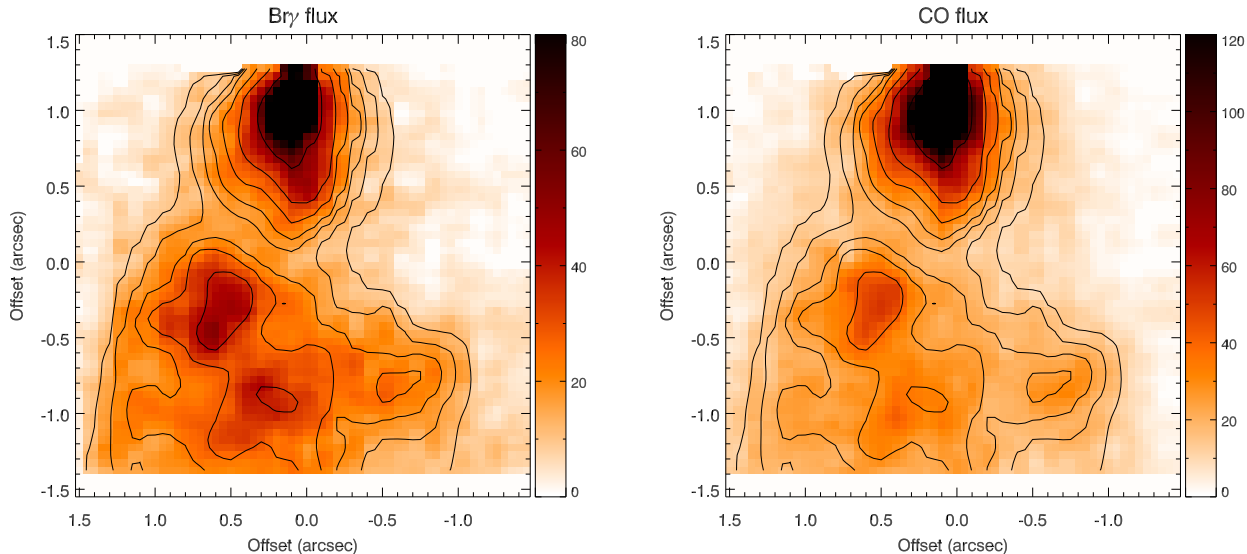


Figure 7. **Left:** Image of the continuum-subtracted line flux of Br γ . The images are scaled in units of sigma above the background, measured from the north-west corner of the image. The overplotted contours show the continuum emission and are drawn at 20σ , 30σ , 40σ , 50σ , 70σ , 100σ and 200σ above the background. **Right:** Same as the left-hand figure but for the first CO bandhead at $2.293\mu\text{m}$.

$2.273\mu\text{m}$, each with a bandwidth of $\pm 0.003\mu\text{m}$. These images were then combined into an RGB image, with the shortest wavelength image assigned to the blue channel and the longest to the red. The resulting image is shown in Fig. 6.

In the image, the southern nebula is seen predominantly in ‘blue’ light (i.e. the shortest wavelength), while the central source appears red. This behaviour can be understood as a combination of scattering and extinction. The central source at region A is heavily absorbed, making the direct light from region A appear red. Meanwhile, the emission to the south is mostly light from region A which has been scattered, and so appears blue.

3.2.3 The Br γ and CO emission

In this section we map the spatial morphology of the emission due to Br γ and CO (the CO absorption is studied in Sect. 3.2.6). First we subtract the continuum at each spatial pixel of the datacube by fitting a 4th-degree polynomial to featureless regions of the continuum. We then integrate the emission across the spectral feature in question. For the CO emission, we took only the bright blue edge of the first bandhead ($2.293\text{--}2.300\mu\text{m}$) – this feature contains the majority of the flux, and is uncontaminated by the low-J absorption lines.

The continuum-subtracted emission images of Br γ and CO are shown in Fig. 7. Both images display morphology similar to that of the continuum image (traced by the contours), with each of the five emission knots clearly visible. It is unlikely that the extended Br γ and CO emission is formed ‘in-situ’ in the southern parts of the nebula, as the two spectral features require different temperatures and densities. It is far more likely that in the southern nebula, as with the continuum emission, we are seeing scattered light which originates within a few AU of the central source.

In Fig. 8 we further explore the scattered light explanation for the Br γ and CO emission by taking the ratio of

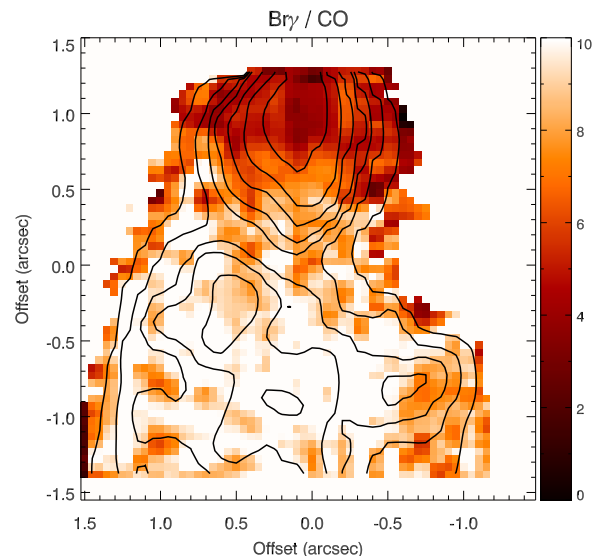


Figure 8. The ratio image of the continuum-subtracted Br γ and CO emission. Contours are the same as those shown in Fig. 7.

the two continuum-subtracted images. If the emission in the southern nebula attributable to these transitions is due to scattering by material in the outflow, we should in principle see very little morphological difference between the emission morphologies. Figure 8 shows that no features corresponding to the southern nebula are seen in the ratio image. Instead, we see a slight increase in the ratio of Br γ to CO in the southern regions compared that around region A. This can be understood as a combination of the wavelength dependence of scattering, which boosts the Br γ /CO ratio in the south, and extinction by dense material around the central source, which attenuates Br γ with respect to CO around region A.

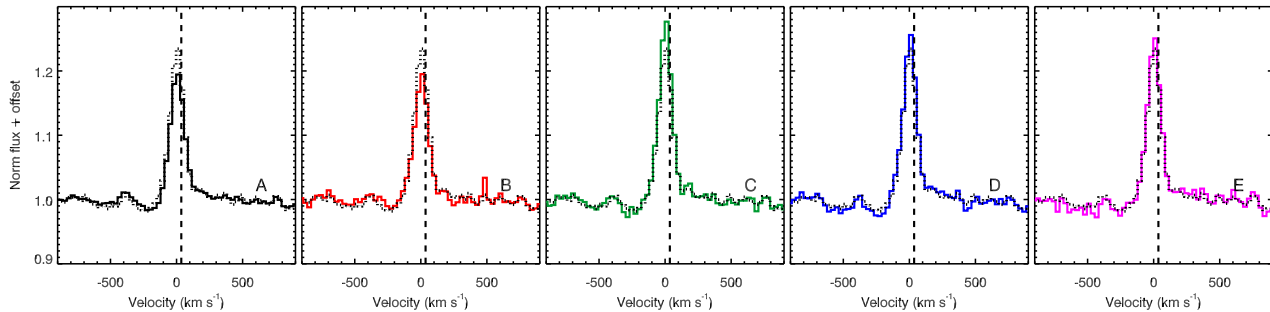


Figure 9. The variations of the Br γ spectral feature across the five bright knots of emission identified in Fig. 3. The mean of the five spectra is overlotted as a dotted line. The dashed line indicates W33A’s systemic velocity.

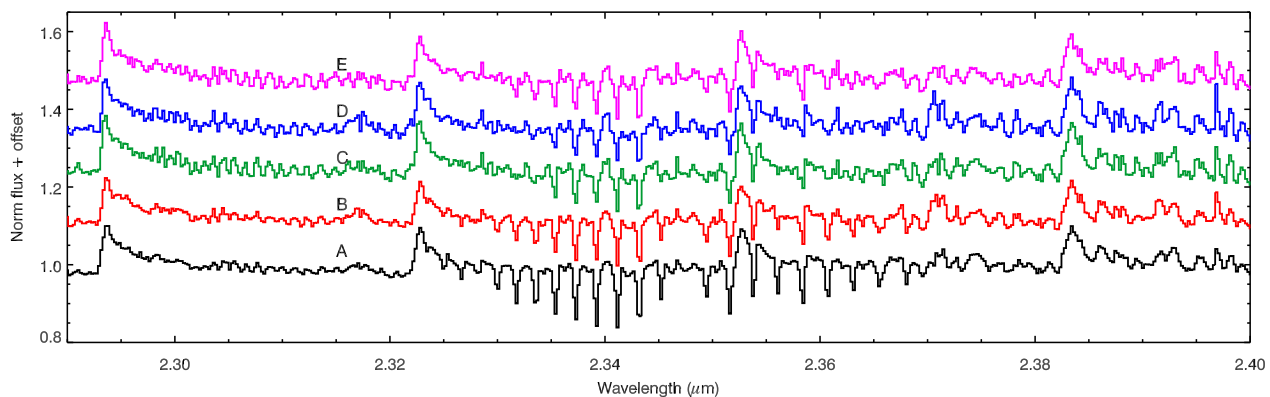


Figure 10. The variations of the CO feature across the five bright knots of emission identified in Fig. 3.

3.2.4 Variations in line-profile with viewing-angle

As we have shown in previous sections, the line-emission observed in the southern nebula is most likely scattered light which originates at the flux centre (i.e. region A). We can then use this scattered light to study the emission from the central source as viewed by the southern nebula, when compared to viewing the emission directly from region A. In effect, this allows us to study the line-profiles as a function of viewing angle. This is a technique we have previously used to study the wind geometry of the evolved massive star IRC +10420 (Davies et al. 2007).

We explore the spatial variations of Br γ and CO in Figs. 9 and 10, where we plot the integrated spectra of the five bright knots of emission identified in Fig. 3 as A-E. In respect to the Br γ emission, there is very little variation across the five regions. The regions show evidence for P Cygni absorption, and perhaps an extended red wing. The equivalent widths (EWs) of the profiles in the southern nebula are slightly larger than those of regions A and B. As the Br γ emission in the southern nebula is most likely scattered light, these small changes in EW are possibly due to anisotropy in the ionized circumstellar gas.

The CO emission shows clear variations across the observed field. To highlight this in Fig. 11 we plot the spectra in the vicinity of the $v=2-0$ bandhead. The blue edge appears shallower in regions A and B, while the edge is much steeper in the three southern regions. Also, the transitions between 2.30-2.305 μm appear to be narrower and more pronounced in the southern knots (C, D and E) than in those close to

region A. This suggests that the CO emission, when viewed directly through the bright central source at region A, has a broadened velocity profile with respect to the profile reflected from the southern nebula. As the southern nebula’s viewing angle to the central source is different from our direct line of sight to the same region, this suggests that the CO profile’s broadening is a function of the viewing angle. Such behaviour is typically attributed to the emission forming in a disk (Bik & Thi 2004a; Blum et al. 2004). As the material in the southern nebula ‘sees’ less rotational broadening than our direct line-of-sight, the orientation of the disk is consistent with being aligned perpendicularly to the larger-scale outflow.

3.2.5 Spectro-astrometry of Br γ

Here we investigate the small-scale geometry of the Br γ emission by performing a 3-D spectro-astrometric analysis of the Br γ line. At each wavelength channel of the datacube we extracted a 2-D image and determined the astrometric centroid of the emission at region A. This method can give spatial information on extremely small scales – the astrometric accuracy on the centroid is roughly equivalent to $\Delta \sim \text{FWHM}/\text{SNR}$. So, for the spatial resolution of our observations (0.13’’) and a SNR at region A of several hundred, in principle we can expect to achieve accuracies of order of a tenth of a milliarcsecond. In order to verify this we performed spectro-astrometric tests on the data from the telluric standards. We found that indeed the r.m.s. on the centroid position was of order 0.1mas. We tried different

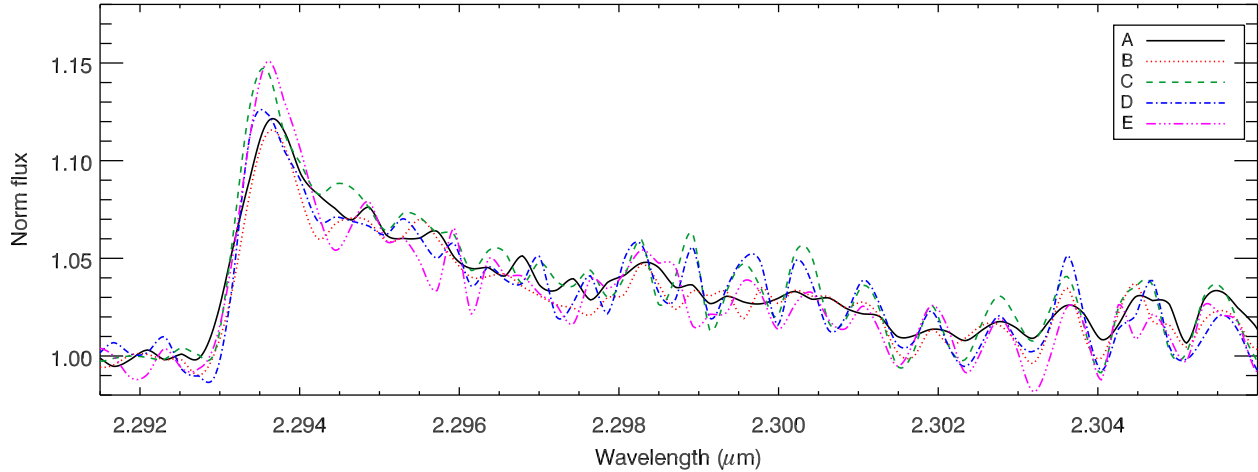


Figure 11. Spectra of the five regions identified in Fig. 3 around the CO $v=2-0$ bandhead. For clarity, spectra have been interpolated onto a finer grid. It is clear from this figure that the line profiles of C, D and E are narrower and more pronounced than those of A and B.

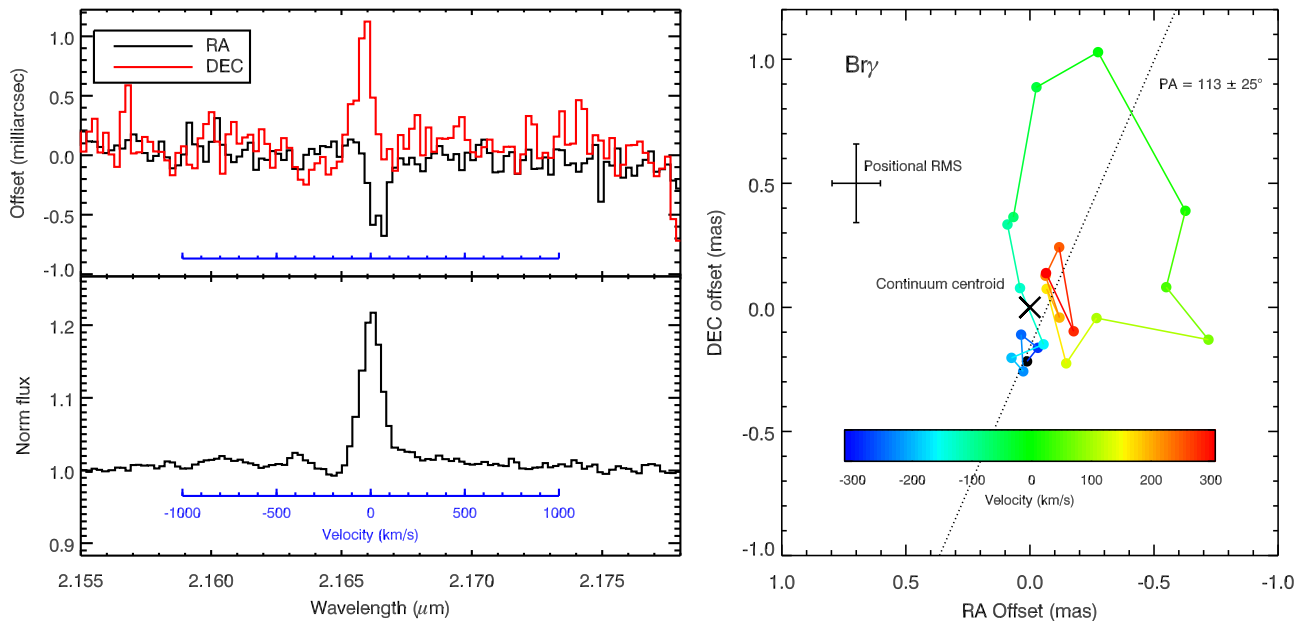


Figure 12. Spectro-astrometry across the Br γ emission line. (**Left**): the bottom panel shows the intensity spectrum of region A, while the top panel shows the astrometric position of the centroid flux peak as a function of wavelength. The red line, labelled ‘DEC’, shows the centroid position in the y -direction, while the black line (‘RA’) shows the position in the x -direction. (**Right**): the same data as in the left-hand panel, but represented in $x - y$ space. The symbols are colour-coded to show the velocity at each point. The dotted line shows the position-angle of the red and blue high-velocity components.

methods of centroiding, including flux-weighted centroiding, finding the location at which the derivatives go to zero and fitting 2-D gaussian profiles. All techniques were found to give similar results within the errors. In addition we observed no artifacts around the telluric absorption lines, and no excursions across the telluric standard star’s intrinsic Br γ absorption, as is to be expected (see Appendix A).

In the left panel of Fig. 12 we plot the position of the centroid as a function of wavelength in the region of Br γ . The spectro-astrometric profiles have had any large-scale gradients removed by fitting a 3rd-degree polynomial to the continuum. Firstly, we note that the astrometric ac-

curacy of the centroid, as judged by the continuum regions, is comparable to that predicted (0.1-0.2mas), corresponding to a physical scale of 0.4-0.8AU for a systemic distance of 3.8kpc. Secondly, the centroid shows a clear shift in the region of Br γ . In the north-south direction (labelled ‘DEC’ in the figure), the centroid appears to shift south slightly in the region of the P Cygni absorption, before shifting northwards by ~ 1 mas. Similarly, in the east-west direction (labelled ‘RA’, where the positive direction is eastward), there is a slight shift to the east coincident with the P Cygni absorption, followed by an excursion to the west of ~ 0.5 mas.

This behaviour is illustrated again in the right panel of

Fig. 12. This time, the centroid is plotted in RA-DEC space with colour-coded symbols to indicate the velocity of each point. The location of the continuum centroid is illustrated by the cross. The plot shows that the emission with the largest red-shifted velocities ($\sim 400 \text{ km s}^{-1}$) is located to the north-west of the continuum location, while the emission blue-shifted by a similar amount is located to the south-east of the continuum, indicating expansion. From analysis of those points with speeds between $300\text{--}400 \text{ km s}^{-1}$ we find that the statistical significance of the red- and blue-shifted points being spatially separated from the continuum is 2.8σ and 4.1σ respectively. In addition to this behaviour there is a large excursion across the centre of the line with $|v| < 100 \text{ km s}^{-1}$.

The observed behaviour can be explained if we make the assumption that the $\text{Br } \gamma$ emission line is made up of two or more components. The broad high-velocity emission originates in an axisymmetric structure, most likely a bipolar jet, while the narrow low velocity emission is formed in an extended structure such as a small, dense H II -region. The nature of this narrow emission is difficult to disentangle, but it is possible that it is formed in an aspherical clumpy medium with much velocity-dependent extinction and self-absorption. This is similar to the picture deduced by Drew et al. (1993) and Bunn et al. (1995) from velocity-resolved line-profile ratios.

In addition to the detection of an outflow, the spectroastrometric data also indicate that the bright flux maximum observed in the integrated image is indeed the location of the central star.

For the broad-line component of the emission we can measure the PA of this structure by taking the data at $300 < |v/\text{km s}^{-1}| < 400$ and taking the mean positions of the red- and blue-shifted components. We measure the PA of this structure to be $113 \pm 25^\circ$ (see right panel of Fig. 12), and so is aligned with the large-scale outflow seen in Fig. 1 (PA= $135 \pm 5^\circ$). From the alignment of these angles it is likely that in this small-scale structure we are seeing the base of a bi-polar ionized wind or jet. In addition, the blue-shifted portion of the $\text{Br } \gamma$ emission is oriented towards the south-east, consistent with the hypothesis that the outflow seen in the wide-field image is the lobe coming towards us, while the red-shifted lobe to the north-west is largely obscured.

The outflow velocity, as measured from Fig. 12, appears to be around $v_{\text{outflow}} \cos i \sim 300 \text{ km s}^{-1}$. Assuming an inclination of 60° (de Wit et al., 2009 submitted), this gives an outflow velocity measured from $\text{Br } \gamma$ of $\sim 600 \text{ km s}^{-1}$. This is likely an underestimate of the outflow's terminal velocity, as a large fraction of the $\text{Br } \gamma$ emission may form in the accelerating part of the wind. This value is consistent with MYSO jet velocities measured by radio proper motion studies (Marti et al. 1998; Curiel et al. 2006).

3.2.6 The CO absorption

The low-J transitions of the CO $v=2-0$ state are observed in absorption in W33A's spectrum (Sect. 3.2). The population of these states requires much cooler conditions ($\sim 30 \text{ K}$) than that of the high-J states seen in emission (few $\times 1000 \text{ K}$) (Chandler et al. 1993, 1995; Bik & Thi 2004a). Therefore these two distinct spectral features must arise in different regions – the CO bandhead emission likely originates in ma-

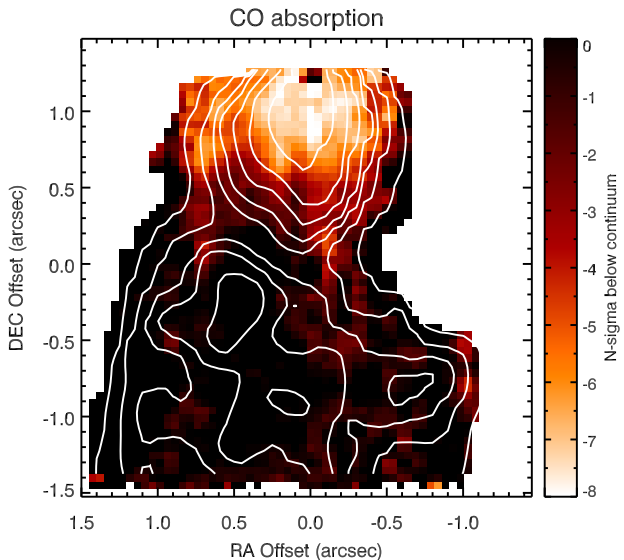


Figure 13. Image of the datacube integrated over the CO absorption lines. The image is scaled in units of sigma below the continuum flux level, where sigma is measured from the southern nebula.

terial close to the central star; while the absorption lines are formed in the outer envelope at several thousand AU (see later).

The right-hand panel of Fig. 9 shows that the CO absorption lines vary in strength between the bright central source (A) and the southern regions (C, D and E). Specifically, the absorption is stronger towards region A than the southern nebula. To explore this behaviour further, sub-cubes were extracted from the primary data-cube, each containing the full spatial information of one of these absorption lines. We observed a behaviour which was similar for each line and so all lines were combined to increase the signal-to-noise.

In Fig. 13 we show the image obtained when the datacube is integrated over these features. The image shows that the CO absorption is concentrated around region A in a band extending roughly east-west, and is perpendicular to the large-scale outflow. Significantly less absorption is seen in the southern nebula, indicating that the material in the southern regions sees less obscuring material than our direct line-of-sight to region A. This suggests that the envelope has the morphology of a torus, with a physical radius of $\sim 2000 \text{ AU}$, and with an opening to the south through which the outflow escapes.

Figure 14 shows the measured velocity centroid of the CO absorption at each spatial position across the extinction structure seen in Fig. 13. The image has been smoothed by a boxcar filter of width 5 pixels to highlight any velocity gradient. At negative (blue-shifted) velocities, the opacity appears to be concentrated in a region about $0.2\text{--}0.3''$ east of the centre of the bright source (i.e. region A). At positive (red-shifted) velocities however, there is a clear shift in the location of the opacity centre to a region $0.1\text{--}0.2''$ west of region A. No apparent trends with velocity are seen in the southern regions of the nebula, though the data are very noisy and are not shown in the figure. We determined the

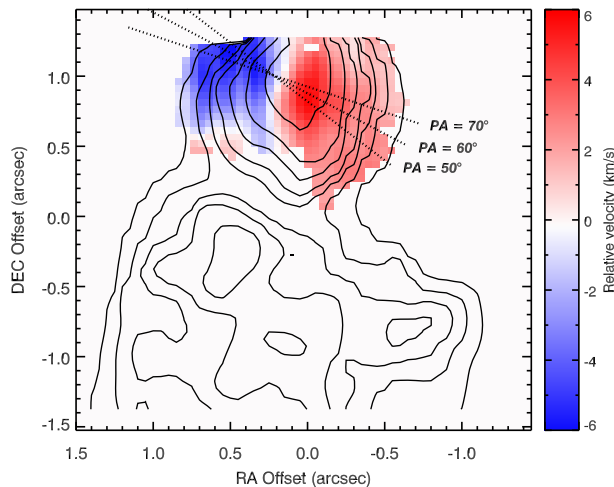


Figure 14. The velocity centroid of the CO absorption lines as a function of spatial position across the field. Velocities are indicated only for those absorption lines which have strengths greater than 5σ below the continuum. The data has been smoothed with a boxcar filter of width 5 pixels ($0.25''$) to accentuate the regions of maximum and minimum velocity. Dotted lines indicate the rough position angle of the structure.

PA of rotation to be $60 \pm 10^\circ$ by fitting the blue and red flux peaks in Fig. 14. This is therefore consistent with being perpendicular to the larger scale outflow of $PA = 135 \pm 5^\circ$. The PA of this feature is perpendicular to the large scale outflow observed in Fig. 1, as well as to the small-scale outflow seen in the spectro-astrometric analysis of the $\text{Br}\gamma$ emission. As with the broadening of the CO bandhead emission described in the previous section, the observed behaviour is indicative of an extended rotating structure seen edge-on. The kinematics of this feature are explored further in Sect. 4.

3.2.7 Molecular hydrogen

The light of H_2 $2.12\mu\text{m}$ shows a very different morphology to that of the continuum and the $\text{Br}\gamma$ and CO emission (see Fig. 15). The emission is concentrated to the south-east of region A, while very little H_2 emission is seen at region A itself. The other H_2 lines observed in the spectrum display similar behaviour, though have much poorer signal-to-noise and so are not shown. The orientation of this emission, extending roughly south-eastwards of region A, is approximately coincident with that of the base of the large-scale outflow seen in the wide-field image of Fig. 1.

4 DISCUSSION – CO KINEMATICS, AND THE MASS OF THE CENTRAL OBJECT

The pieces of evidence presented above are all consistent with the qualitative picture of a massive forming star in which the central object is surrounded by a rotating disk from which it is accreting. A rotationally-flattened envelope surrounds the central star and its disk, while the star drives a fast bi-polar wind.

In this section we present a kinematic analysis of the CO bandhead emission and the low-J CO absorption lines

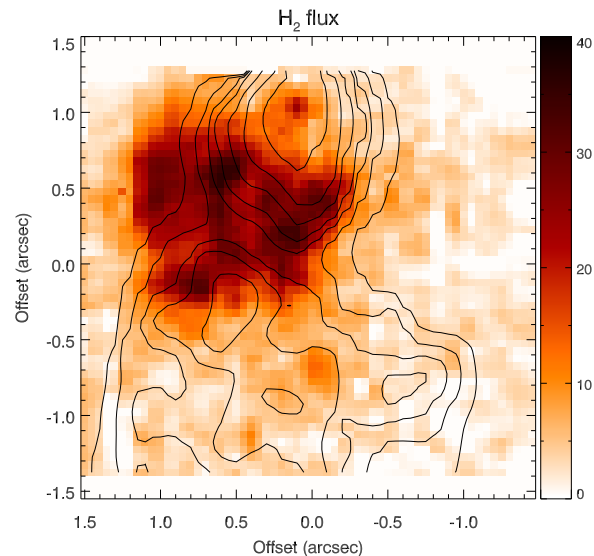


Figure 15. Same as Fig. 7 but for H_2 $2.12\mu\text{m}$. The point-like emission at the very centre of region A is possibly due to poor continuum subtraction.

and use them to derive the mass of the object about which they rotate.

4.1 The bandhead broadening

As shown in Fig. 11, the CO bandhead emission lines appear to be broader towards region ‘A’ than those observed in the southern nebula. This behaviour can be attributed to a flattened rotating structure (i.e. a disk) which is seen at lower inclination when viewed directly than when seen reflected by the nebula to the south. If we assume the extreme case that (a) the line-of-sight ‘A’ views the disk edge-on, and (b) that the southern nebula views the disk pole-on, by convolving the profile seen from the southern nebula until it matches that at ‘A’ we can estimate a lower limit to the disk rotation speed. By assuming Keplerian rotation we can then estimate the mass of the central object about which the disk rotates.

In Fig. 16 we plot the CO bandhead profile seen at ‘A’. We also plot the profile seen in the southern nebula (region ‘C’) which has been convolved with a rotational broadening function of the form $\psi(v) \sim [1 - (v/V_{\text{rot}})^2]^{1/2}$, where v is velocity and V_{rot} is the disk rotational velocity. The best match to the blue-edge of the bandhead, as well as the lower-J line profiles, is found when the rotational velocity is $50 \pm 5 \text{ km s}^{-1}$. If the direct line-of-sight is not exactly edge-on, and/or if the orientation of the reflected light is not exactly pole-on, the disk rotation speed will be greater than this value. By taking the inclination angle recently derived by de Wit et al. (submitted) of $60 \pm 20^\circ$ (i.e. 30° away from being edge-on), we can further constrain the disk rotation speed to $64_{-8}^{+22} \text{ km s}^{-1}$.

Assuming that the disk rotation is Keplerian, and that the CO emission arises in a narrow annulus at a fixed radius R from the central object we can now derive a mass of the central object M_c from,

$$M_c = RV^2/G \quad (1)$$

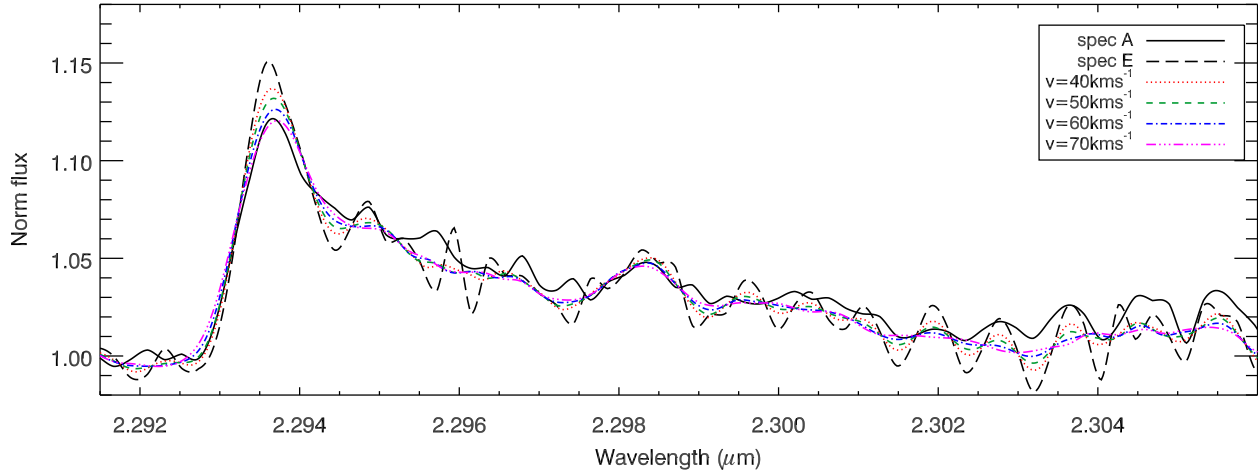


Figure 16. The observed profile of the CO bandhead in region ‘A’ (black solid line), as well as the profile seen in the southern nebula (from region ‘C’) when convolved with a PSF of various widths.

where G is the gravitational constant. Bik & Thi (2004b) who found that the CO typically forms at a distance from the central star of 1-3AU. Using $R = 2 \pm 1$ AU, and a distance to W33A of 3.8kpc (Faúndez et al. 2004), we find that the lower limit to the central mass is $M_c = 10_{-5}^{+9} M_\odot$.

4.2 The absorption-line velocity structure

In Sect. 3.2.6 we showed that the absorption lines of CO appear to be formed in a rotating structure coincident with region A, and measured the PA of this structure to be $60 \pm 10^\circ$. In Fig. 17 we show a position-velocity slice across the averaged CO datacube at a PA of 60° . The data shows the classical signature of a Keplerian rotating structure. To help illustrate this, overplotted are models of Keplerian rotation for three different central masses and with an assumed distance of 3.8kpc (Faúndez et al. 2004). Each curve has been convolved with the spatial resolution of our observations ($0.13''$). A formal least-squares fit to the data yields a central mass of $M \sin i = 13 \pm 2 M_\odot$, a result which is insensitive to the uncertainty in PA. If we again assume the system inclination is $60 \pm 20^\circ$ we find that the outer envelope sees a central mass of $15_{-3}^{+5} M_\odot$. Note that the central mass seen by the envelope will include the mass of the envelope itself. This number is very similar to that derived for the central mass enclosed by the circumstellar disk, and suggests that the majority of the system’s mass is contained within the central star.

If the central object has arrived on the main-sequence, this mass would correspond to a spectral type earlier than B1 and a zero-age min-sequence luminosity of $\log(L/L_\odot) = 4.3 \pm 0.3$ (e.g. Meynet & Maeder 2000). This is in good agreement with the latest estimation of W33A’s bolometric luminosity from MIPS photometry, $\log(L/L_\odot) = 4.7$ (Mottram et al. 2009, in prep). The derived spectral-type and luminosity may also explain the detection of the Mg II emission lines. Such lines are typically seen in the spectra of early-to-mid B supergiants, and are primarily formed in the wind (Hanson et al. 2005). The ionization emission lines that we see in W33A (Br γ and Mg II) are probably formed in the bi-

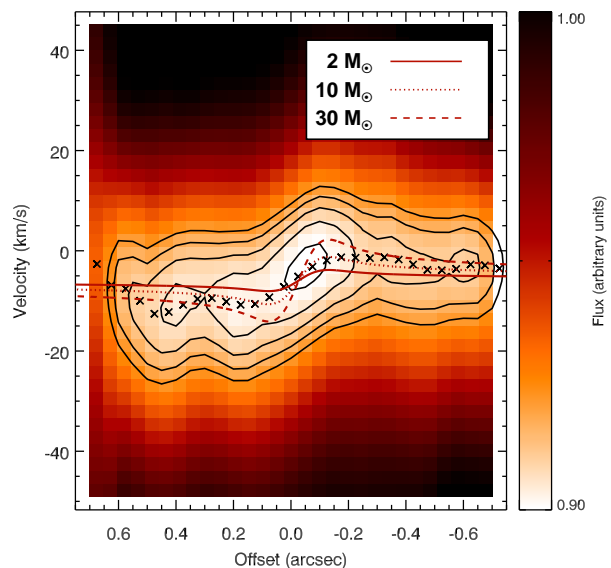


Figure 17. Position-velocity diagram across the rotating structure seen in the CO absorption lines. The image is scaled in terms of fractional intensity below the continuum. The crosses indicate the velocity of the intensity minimum for the absorption as a function of positional offset, and contours are drawn at intensity levels of 0.895 to 0.92 at intervals of 0.005. Lines show models of Keplerian rotation for three different central masses and an assumed distance of 3.8kpc.

polar outflow, the density of which may be similar to that of a typical B supergiant wind.

5 SUMMARY AND CONCLUSIONS

We have presented a study of adaptive-optics assisted near-infrared integral-field spectroscopy of the young stellar object W33A. The results can be summarized as follows:

- In the first 3-D spectro-astrometric study of its kind, we have resolved the Br γ emission on sub-milliarcsecond scales

(physical scales <1 AU), and find that the emission geometry is that of a fast bipolar wind which is aligned with the large-scale outflow seen in wide-field images. The H_2 $2.12\mu\text{m}$ emission also traces an outflow with the same orientation out to $\sim 1''$.

- The extended nebulosity to the south is seen in the continuum, as well as in the light of $\text{Br}\gamma$ and CO. We have shown that this emission is light reflected by the outflow lobe, and so can be used as a ‘mirror’ with which to observe the emission from the central object from different angles.

- We interpret the CO emission as arising in a disk which has a low inclination with respect to our line-of-sight. In the southern nebula we see light reflected towards us from the disk at a lower inclination angle (i.e. more pole-on), which causes the bandhead profile to be less velocity-broadened. This is consistent with the disk plane being perpendicular to the large-scale outflow. The velocity broadening implies a lower-limit to the central mass of $M_c = 10^{+9}_{-5} M_\odot$.

- From the low-J $v=2-0$ transitions of CO at $\sim 2.35\mu\text{m}$ we find evidence for a rotationally-flattened cool molecular envelope, or ‘torus’, at a radius of ~ 2000 AU from the central star. The plane of rotation is perpendicular to the small- and large-scale outflows. Analysis of the velocity structure of the torus indicates that it is rotating about the outflow’s axis, and that it is orbiting a central mass of $15^{+5}_{-3} M_\odot$.

Our findings suggest a picture of massive star formation within W33A which is in excellent qualitative agreement with the accretion-disk-plus-bipolar wind paradigm. An accretion disk orbits a massive central star, which is surrounded by a cool molecular envelope which has been rotationally-flattened into a torus. The central star is driving a bipolar wind, seen on small scales in the ionized gas, and on larger scales as molecular / continuum emission. The two measurements of the central mass indicate that at most the accretion disk makes up $\sim 30\%$ of the system, and so the system mass is dominated by the central star.

ACKNOWLEDGMENTS

Based on observations obtained at the Gemini Observatory, which is operated by the Association of Universities for Research in Astronomy, Inc., under a cooperative agreement with the NSF on behalf of the Gemini partnership: the National Science Foundation (United States), the Science and Technology Facilities Council (United Kingdom), the National Research Council (Canada), CONICYT (Chile), the Australian Research Council (Australia), Ministério da Ciência e Tecnologia (Brazil) and Ministerio de Ciencia, Tecnología e Innovación Productiva (Argentina).

REFERENCES

Beltrán, M. T., Cesaroni, R., Codella, C., Testi, L., Furuya, R. S., & Olmi, L. 2006, *Nature*, 443, 427
 Beuther, H., Churchwell, E. B., McKee, C. F., & Tan, J. C. 2007, in *Protostars and Planets V*, ed. B. Reipurth, D. Jewitt, & K. Keil, 165–180
 Beuther, H., Schilke, P., Sridharan, T. K., Menten, K. M., Walmsley, C. M., & Wyrowski, F. 2002, *A&A*, 383, 892
 Bik, A. & Thi, W. F. 2004a, *A&A*, 427, L13

—. 2004b, *A&A*, 427, L13
 Blum, R. D., Barbosa, C. L., Damineli, A., Conti, P. S., & Ridgway, S. 2004, *ApJ*, 617, 1167
 Bunn, J. C., Hoare, M. G., & Drew, J. E. 1995, *MNRAS*, 272, 346
 Chandler, C. J., Carlstrom, J. E., & Scoville, N. Z. 1995, *ApJ*, 446, 793
 Chandler, C. J., Carlstrom, J. E., Scoville, N. Z., Dent, W. R. F., & Geballe, T. R. 1993, *ApJ*, 412, L71
 Curiel, S., Ho, P. T. P., Patel, N. A., Torrelles, J. M., Rodríguez, L. F., Trinidad, M. A., Cantó, J., Hernández, L., Gómez, J. F., Garay, G., & Anglada, G. 2006, *ApJ*, 638, 878
 Davies, B., Oudmaijer, R. D., & Sahu, K. C. 2007, *ApJ*, 671, 2059
 de Wit, W. J., Hoare, M. G., Oudmaijer, R. D., & Mottram, J. C. 2007, *ApJ*, 671, L169
 Drew, J. E., Bunn, J. C., & Hoare, M. G. 1993, *MNRAS*, 265, 12
 Faúndez, S., Bronfman, L., Garay, G., Chini, R., Nyman, L.-Å., & May, J. 2004, *A&A*, 426, 97
 Gibb, E. L., Whittet, D. C. B., Schutte, W. A., Boogert, A. C. A., Chiar, J. E., Ehrenfreund, P., Gerakines, P. A., Keane, J. V., Tielens, A. G. G. M., van Dishoeck, E. F., & Kerkhof, O. 2000, *ApJ*, 536, 347
 Hanson, M. M., Kudritzki, R.-P., Kenworthy, M. A., Puls, J., & Tokunaga, A. T. 2005, *ApJS*, 161, 154
 Hoare, M. G., Kurtz, S. E., Lizano, S., Keto, E., & Hofner, P. 2007, in *Protostars and Planets V*, ed. B. Reipurth, D. Jewitt, & K. Keil, 181–196
 Krumholz, M. R., Klein, R. I., McKee, C. F., Offner, S. S. R., & Cunningham, A. J. 2009, *Science*, 323, 754
 Lucas, P. W., Hoare, M. G., Longmore, A., Schröder, A. C., Davis, C. J., Adamson, A., Bandyopadhyay, R. M., de Grijs, R., Smith, M., Gosling, A., Mitchison, S., Gáspár, A., Coe, M., Tamura, M., Parker, Q., Irwin, M., Hambly, N., Bryant, J., Collins, R. S., Cross, N., Evans, D. W., Gonzalez-Solares, E., Hodgkin, S., Lewis, J., Read, M., Riello, M., Sutorius, E. T. W., Lawrence, A., Drew, J. E., Dye, S., & Thompson, M. A. 2008, *MNRAS*, 391, 136
 Marti, J., Rodríguez, L. F., & Reipurth, B. 1998, *ApJ*, 502, 337
 McGregor, P. J., Hart, J., Conroy, P. G., Pfitzner, M. L., Bloxham, G. J., Jones, D. J., Downing, M. D., Dawson, M., Young, P., Jarnyk, M., & Van Harmelen, J. 2003, in *Society of Photo-Optical Instrumentation Engineers (SPIE) Conference Series*, Vol. 4841, Society of Photo-Optical Instrumentation Engineers (SPIE) Conference Series, ed. M. Iye & A. F. M. Moorwood, 1581–1591
 Meynet, G. & Maeder, A. 2000, *A&A*, 361, 101
 Parkin, E. R., Pittard, J. M., Hoare, M. G., Wright, N. J., & Drake, J. J. 2009, *MNRAS*, 1372
 Patel, N. A., Curiel, S., Sridharan, T. K., Zhang, Q., Hunter, T. R., Ho, P. T. P., Torrelles, J. M., Moran, J. M., Gómez, J. F., & Anglada, G. 2005, *Nature*, 437, 109
 Rengarajan, T. N. & Ho, P. T. P. 1996, *ApJ*, 465, 363
 Taban, I. M., Schutte, W. A., Pontoppidan, K. M., & van Dishoeck, E. F. 2003, *A&A*, 399, 169
 Torrelles, J. M., Patel, N. A., Curiel, S., Ho, P. T. P., Garay, G., & Rodríguez, L. F. 2007, *ApJ*, 666, L37
 van der Tak, F. F. S. & Menten, K. M. 2005, *A&A*, 437, 947

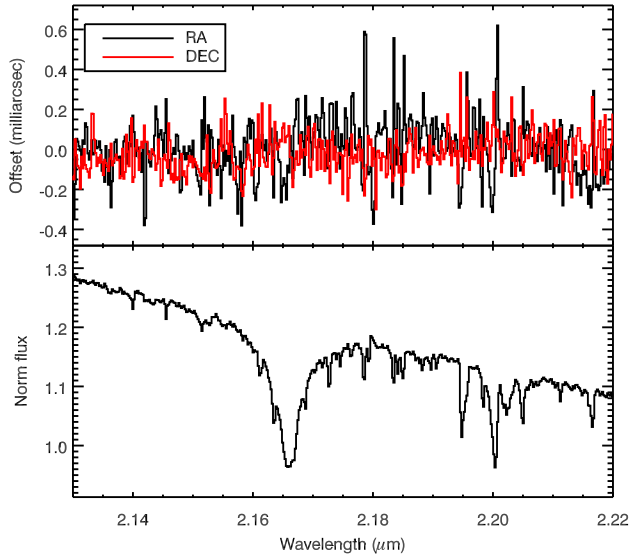


Figure A1. Spectro-astrometry of the $\text{Br } \gamma$ line for the telluric standard star used in our observations, similar to Fig. 12. The lack of artifacts across the telluric features and the star's $\text{Br } \gamma$ absorption, as well as the observed level of astrometric precision ($\sim 0.2\text{mas}$), validate the results of the similar analysis of W33A.

Yorke, H. W. & Sonnhalter, C. 2002, ApJ, 569, 846

APPENDIX A: SPECTRO-ASTROMETRY OF THE TELLURIC STANDARD STAR

In Fig. A1 we show a spectro-astrometric analysis of the telluric standard star following a similar methodology to that presented in Sect. 3.2.5. The intensity spectrum (bottom panel) shows the $\text{Br } \gamma$ absorption line, as well as the many telluric features. The top panel shows the astrometry of the star's flux peak as a function of wavelength, illustrating that no discernable variations are seen across neither the $\text{Br } \gamma$ line nor the telluric lines. This of course is to be expected, and the Figure serves to show that the technique we employ produces no spurious artifacts greater than the noise level ($\sim 0.2\text{mas}$) which could be misinterpreted.